Compliance Boundary Conditions for Simulating Deformations in a Limited Target Region

Ece Ozkan[1] and Orcun Goksel[1]

Abstract— **Patient-specific models in medical procedures are often limited to a relatively small region of interest due either to computational concerns or to the fact that only a part of anatomy could be observed in the input medical images. Thus, for deformable planning or training simulations, boundary conditions at the borders of such models are necessitated. Zero-displacement or -force constraints at outer boundaries are commonly used, with the assumption that the selected region is large enough to minimize effects on the deformable behavior inside the region of interest. This may, however, still result in errors and does require superfluous elements to extend models. In this work, a mixed boundary condition type, called compliance boundary condition, is proposed to constrain model boundaries. Different techniques to define and estimate these boundary constraints are studied with simulation experiments. Results are presented for palpation on 2D and 3D phantoms and needle insertion to a male pelvic anatomical model.**

I. INTRODUCTION

Medical simulations are essential for planning and training of interventions. For an accurate simulation, patient-specific models are necessitated. For deformation simulation, these models consist of a spatial map of one or more deformation parameters in or near the anatomical region of interest, based on which one can compute the deformable tissue reaction together with an interaction model [7], [11]. Finite Element Method (FEM) is a popular continuum-mechanics based technique, in which the region is discretized into simple geometric elements. Together with their deformable parametrization (e.g. Young's or elastic modulus) and fixation in space (through boundary constraints), one can then compute the deformable response of the model by solving partial differential equations. Other popular models use mass-spring and finite difference methods.

Patient-specific deformable models involve a combination of a geometric model, its parametrization, and boundary constraints. Geometric models are generally in the form triangulated surfaces separating different presumably-homogeneous anatomical regions, often delineated from medical images such as CT or MRI, e.g. [10]. Then, typically empirical deformable parameters from the literature are assigned in those regions. An imaging technique, called *elastography*, can enable the estimation of local deformable parameters [9], [2], which may be used to parameterize patient-specific deformation models. Despite numerous works in the literature on recovering geometry and/or spatial parametrization of deformable tissue, there is little to no work on defining accurate boundary constraints. This is despite the well-known fact that boundary conditions often play a much larger role in the deformation outcome than discretization parametrizations [14], [12]. In this work, a novel model for *parameterized boundary conditions* is proposed, which can be represented naturally in the standard FEM framework (embedded in the stiffness matrix formulations), and methods to estimate such boundary conditions are introduced.

For deformable models, skeletal system is often considered as a fixed boundary condition, as been grounded to the patient table. For instance, during breast biopsy, the rib-cage can be taken as a fixed wall [8]; or for the prostate, the pelvic bone is considered fixed [11]. Patient-specific models used in medical simulations often do not cover the extent of the entire body, but instead focus on a smaller region-of-interest (ROI), due mainly to the limited field-of-view of image acquisition systems or due to computational constraints. Therefore, the ideal case is when such ROI is severed from the rest of the body by some anatomical boundary that is within the ROI; e.g., by just imaging the breast and the rib cage, one can ignore the rest of the body. However, for abdominal anatomy, this is often not the case, and all organs interact at some level with each other, i.e. breathing from the diaphragm can be visible in the prostate region. Consequently, when a small ROI is taken around an abdominal organ, its interaction with the rest of the abdomen and thorax cannot be ignored. Nevertheless, to the best of the authors' knowledge, most simulations to date ignore such interaction, and simply employ a zero-displacement (as if the ROI is "glued" within a box or sphere) or a zero-force (as if the borders of the ROI are the skin in the air) boundary constraints [1], [11]. Some studies first pad the actual ROI with superfluous tissue (FEM elements) in order to dissipate the effects of zero-displacement or -force constraints at the outer boundaries [6], [13]. Nevertheless, how far and with which tissue to pad are outstanding questions, with no guarantees on this representing the real deformations, let alone the additional computational burden brought by the extended model.

In this work, we introduce a novel formulation of boundary constraints in a way that can be naturally represented and solved in the standard FEM framework. We also present techniques to parametrize such boundary conditions experimentally from observed tissue displacements, which can be acquired using medical imaging, e.g. MRI and ultrasound. For the purpose of this paper, we simulate such observations from known ground-truth models of larger anatomy.

Note that, *compliance boundary conditions* are indeed

*This work is supported by the Swiss National Science Foundation.

[1]Computer-assisted Applications in Medicine Group, Computer Vision Lab, ETH Zurich, Switzerland

a generalization of the boundary conditions introduced in [5], in which springs of empirically-set stiffness and infinite length are attached to boundary nodes in order to couple separate models. Here, we propose an approach to have more complex boundary conditions as well as experimentally parametrize those by exploiting observed deformations.

II. METHODS

Considering a linearly-elastic ROI discretized by N mesh nodes into FE, the relation between the nodal elastic forces $\mathbf{f}$ and the nodal displacements $\mathbf{u}$ of this model is characterized by the FEM through the following linear system: $\mathbf{K}\mathbf{u} = \mathbf{f}$, where $\mathbf{K}$ is the stiffness matrix dependent on the geometry and biomechanical properties of the elements. In order to set up our problem formally, below we will first consider that a deformable model of the entire anatomical extent exists and is given to us. Based on this, we will first show its relation to a limited-ROI stiffness-matrix $\mathbf{K}$, and then introduce different approximation models to such relation. We then present methods to parametrize such models, while considering experimental limitations, e.g. observation noise.

A. Relation to a Full Anatomical Model

Let us first consider that a full model of the entire anatomy is known (given). Although this in fact will never be the case in reality, it will still help us below to define a formal relation of such full model $\mathbf{K}_\mathrm{f}$ to the ROI boundary conditions. Consider the deformable full FEM model with nodes reordered such that *observed* nodes in the ROI come first and *unobserved* nodes follow next, i.e.:

$$\mathbf{K}_\mathrm{f}\mathbf{u}_\mathrm{f} = \begin{bmatrix}\mathbf{K}_\mathrm{oo} & \mathbf{K}_\mathrm{ou}\\ \mathbf{K}_\mathrm{uo} & \mathbf{K}_\mathrm{uu}\end{bmatrix}\begin{bmatrix}\mathbf{u}_\mathrm{o}\\ \mathbf{u}_\mathrm{u}\end{bmatrix} = \begin{bmatrix}\mathbf{f}_\mathrm{o}\\ \mathbf{f}_\mathrm{u}\end{bmatrix} = \mathbf{f}_\mathrm{f}. \tag{1}$$

From $\mathbf{f}_\mathrm{u} = \mathbf{K}_\mathrm{uo}\mathbf{u}_\mathrm{o} + \mathbf{K}_\mathrm{uu}\mathbf{u}_\mathrm{u}$, it follows that:

$$\mathbf{u}_\mathrm{u} = \mathbf{K}_\mathrm{uu}^{-1}\left(\mathbf{f}_\mathrm{u} - \mathbf{K}_\mathrm{uo}\mathbf{u}_\mathrm{o}\right) \tag{2}$$

and replacing (2) in (1) and algebraic manipulations yield:

$$\underbrace{\mathbf{f}_\mathrm{o} - \mathbf{K}_\mathrm{ou}\mathbf{K}_\mathrm{uu}^{-1}\mathbf{f}_\mathrm{u}}_{\tilde{\mathbf{f}}_\mathrm{o}} = \underbrace{\left(\mathbf{K}_\mathrm{oo} - \mathbf{K}_\mathrm{ou}\mathbf{K}_\mathrm{uu}^{-1}\mathbf{K}_\mathrm{uo}\right)}_{\tilde{\mathbf{K}}_\mathrm{oo}}\mathbf{u}_\mathrm{o}, \tag{3}$$

where $\tilde{\mathbf{K}}_\mathrm{oo}$ is the so called *condensed* stiffness matrix [3]. For instance, the condensed matrix for the (green) ROI in the 2D example in Fig. 1(a) looks as in Fig.1(b)(top). This N node system in (3) indeed models the ROI deformation *exactly* as if the entire anatomical model were present. However, without the geometry and parameters of the full model, which are not always readily available or observable in practice, then $\tilde{\mathbf{K}}_\mathrm{oo}$ can also not be deduced. Nevertheless, if one can observe and model the ROI, i.e. $\mathbf{K}$, then we can try to estimate the incremental difference $\mathbf{C}$ between that and the condensed system, i.e. $\mathbf{C} = \tilde{\mathbf{K}}_\mathrm{oo} - \mathbf{K}$. For the 2D example in Fig. 1(a), such difference $\mathbf{C}$ would look as in Fig. 1(b)(bottom). Our motivation is that $\mathbf{C}$ can be approximated from few observed deformations. This will then enable augmenting $\mathbf{K}$ to an *approximate* condensed system, using which any interaction response can be computed similarly to the response of the unknown full system. Since $\mathbf{C}$ then encodes the effects of boundary conditions on $\mathbf{K}$ that are neither zero-displacement nor zero-force, but rather *compliant* (spring-like), we call this augmentation as *compliance boundary constraints*.

B. Estimating Compliance Boundaries

Assuming no external force is applied on unobserved nodes, i.e. $\mathbf{f}_\mathrm{u} = 0$, then (3) becomes $\mathbf{f}_\mathrm{o} = \left(\mathbf{K} + \mathbf{C}\right)\mathbf{u}_\mathrm{o}$. Since the forces on all nodes except the ones that are manipulated are zero, we can solve this system for such rows, i.e.:

$$\left(\mathbf{K}' + \mathbf{C}'\right)\mathbf{u}_\mathrm{o} = \mathbf{0} \tag{4}$$

$$\mathbf{C}'\mathbf{u}_\mathrm{o} = -\mathbf{K}'\mathbf{u}_\mathrm{o}, \tag{5}$$

where prime indicates that the few rows corresponding to manipulated nodes are removed. Note that $\mathbf{C}$ has non-zero elements only for row/columns corresponding to the ROI boundary nodes, thus unless a boundary was manipulated, such dropped rows do not lose unknowns from $\mathbf{C}$. Additionally, for known tissue composition (e.g. patient-specifically modeled or imaged by elastography) and for observed displacements $\mathbf{u}_\mathrm{o}$, the right-hand-side of (5) is known – represented hereafter with the column vector $\mathbf{b}$.

Since $\mathbf{C}$ has several unknowns, but the observations cannot be arbitrarily many, solving the full $\mathbf{C}$ matrix is unrealistic in practice. Nevertheless, intuitively and as also empirically observed, many nonzero elements are on the block diagonal of C, e.g. 49% of the elements in Fig. 1(b) (bottom). For a block-diagonal approximation (*block*), each boundary node in (5) becomes linearly independent, leading for node i to:

$$\begin{bmatrix}c_{i,1} & c_{i,3}\\ c_{i,3} & c_{i,2}\end{bmatrix}\begin{bmatrix}u_{\mathrm{o,ix}}\\ u_{\mathrm{o,iy}}\end{bmatrix} = \begin{bmatrix}b_{\mathrm{i,x}}\\ b_{\mathrm{i,y}}\end{bmatrix} \tag{6}$$

For given observations, constraints at boundary nodes can then be approximated as the solution of the linear system:

$$\begin{bmatrix}u_{o,ix} & u_{o,iy} & 0\\ 0 & u_{o,ix} & u_{o,iy}\end{bmatrix}\begin{bmatrix}c_{i,1}\\ c_{i,2}\\ c_{i,3}\end{bmatrix} = \begin{bmatrix}b_{\mathrm{i,x}}\\ b_{\mathrm{i,y}}\end{bmatrix} \tag{7}$$

solved via pseudo-inverse. As each observation has x and y components, we need at least two observations (e.g. motion-tracked palpations) to uniquely solve for *block* unknowns.

A simpler approximation is just to solve for the diagonal elements; e.g. Fig. 1(b)(bottom) has 45% of non-zero elements on the diagonal. Diagonal elements $c_{i,1}$ and $c_{i,2}$ corresponding to each row can be estimated with the above linear system, where $c_{i,3}$ is then assumed to be zero. This indeed corresponds to an axis-aligned compliant (spring) model as shown in Fig. 1(c). Note that only one observation is sufficient to reconstruct *diag C* model in 2D.

III. RESULTS

To study the proposed techniques above, we used a simple palpation experiment in 2D and 3D numerical phantoms, as well as a needle insertion example on a male pelvic anatomical model. We applied palpations and obtained the deformation of the model from the FEM. In each experiment, we had the (entire) full FEM model, $\mathscr{M}_\mathrm{f}$, within which we

attempted to estimate a reduced model, $\mathscr{M}_\mathrm{r}$, in a smaller ROI. This ROI is selected considering where interactions are carried out and deformations are of interest, as well as for feasibility for imaging to get observations, e.g. near the surface assuming ultrasound acquisition.

In an observation phase, we utilized $\mathscr{M}_\mathrm{f}$ to mimic the acquisition of deformation response, e.g., by some imaging technique. For given interactions we observed the deformations within the ROI and used those to estimate compliance boundary conditions as mentioned above. Additionally, $\mathscr{M}_\mathrm{f}$ was utilized also for generating ground-truth deformations such that the results approximated by our models could be evaluated. Accordingly, for other random interactions (e.g. the palpation at a different surface location) the nodal displacements $\mathbf{d}$ were calculated from $\mathscr{M}_\mathrm{f}$ and compared to the displacements $\mathbf{u}$ of the reduced model $\mathscr{M}_\mathrm{r}$ for that interaction. The average error is reported as the average at all nodes in the ROI, by normalizing to the maximum nodal displacement (often the palpation/interaction magnitude) d_0, i.e. $\delta = \frac{\sum_{i=1}^{N} \delta_i}{N \cdot d_0}$, where δ_i is the Euclidean distance between the estimated and ground-truth displacements at node i.

A. Experimental Setup

In 2D, a 140×160 mm full numerical phantom with a depth of 10 mm was constructed, where a $60\times80\times10$ mm part is defined as the ROI, as seen in Fig. 1(a). Deformation was modeled using linear triangular FEM elements. There were 479 nodes in the full model and 111 nodes in the ROI. In 3D, a $140\times140\times160$ mm numerical phantom (with 3825 nodes) was constructed with linear tetrahedral elements, with a $60\times60\times80$ mm surface section (of 41 nodes) being the ROI. Poisson's ratio was set to 0.49 and Young's modulus to 10 kPa. Compressions of 0.3% strain (of full depth) were applied for observation and evaluation. The full models were assumed to have zero-displacement constraint at their bottom surface. Two baseline comparisons for reduced model were done; first, zero-displacement constraint for bottom surface in all directions (*bottom*) and, second, additional zero-displacement constraints for side surfaces were used only in the normal direction (*all fix*).

Male pelvic model was acquired from segmented MR images. The full model had an extent of $131\times185\times137$ mm, meshed with 3499 nodes and 16239 tetrahedral elements, including models of the prostate, bladder, pelvic bone, and remaining soft tissue as seen in Fig. 2(a). For the reduced model, we considered a region from the skin to the prostate, where the needle interaction and relevant prostate deformation occur. This yielded 345 nodes and 1197 tetrahedral elements as seen in Fig. 2(b). Poisson's ratio was set to 0.49. Young's modulus was set to 20 kPa for the prostate, 10 kPa for the bladder, and 15 kPa for the remaining elements as in [4]. Nodes on the pelvic bone were set as zero-displacement constraints for both full and reduced models. Again, two baseline comparisons for reduced model were performed; first, zero-displacement constraints for nodes on pelvic bone (*only bone*) and, second, zero-displacement constraints on all surfaces except the skin on inferior side were used (*all*).

B. Ideal (Noise-free) Observations

First, we studied noise-free observations, ignoring potential imaging and motion estimation errors in an experimental setup. We first tested in 2D an ideal scenario, in which the interaction during the observations will be exactly on the same location (nodes) as the interactions during the experiments, called *same* in the results. Note that in the linear (Hookean) deformation model that we use, this first simple example can be simulated without requiring boundary condition estimation, as the response for interactions on the same nodes would scale linearly and can simply be estimated as a linear combination of the observations. Later, we used a more realistic scenario where the interaction location on the reduced model is different (not known a-priori), called *diff1* in the results. At some selected surface nodes, several palpations $d_i = [d_{i,x}, d_{i,y}]^T$ were applied corresponding to different observations and evaluations with $d_{i,x} = d_0 \cos(\pi i/M)$ and $d_{i,y} = d \sin(\pi i/M)$ for a total number of M observations and evaluations. Table I(A) shows the error for compliance boundary conditions (CBC) and conventional (empirical) BC setting, where three observations were used and seven evaluations were performed. *diag* is seen to yield best results.

We also studied the effect of the number of linearly-independent observations on average error. Note that increasing M does not necessarily yield more linearly-independent observations, as each observation is a linear combination of $M-1$ others. For obtaining linearly-independent observations, interactions were performed on different node combinations, called *diff2* in the results Table I(A). It is seen as expected that increasing number of linearly-independent observations decreases the average error for *block* more significantly than *diag*, since *block* is a more expressive model

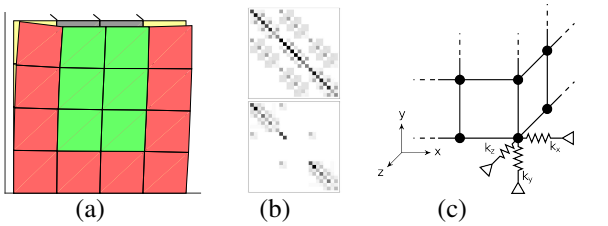

(a) (b) (c)

Fig. 1. In (a) bottom surface of the full model is fixed and top surface of the reduced model is pushed. The nodes in orange part are unknown and in green part are observed ROI nodes. In (b) (top) $\bar{\mathbf{K}}_{\mathrm{oo}}$ and (down) $\mathbf{C}$ and in (c) the compliance boundary conditions for *diag* approximation is shown.

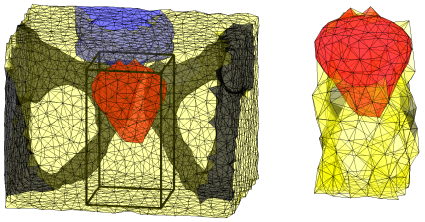

(a) (b)

Fig. 2. In (a) full model of male pelvic anatomy is shown with soft tissue (yellow), pelvic bone (gray), bladder (blue) and prostate (red). Bounding box shows the ROI, also zoomed in (b).

with higher degrees-of-freedom, meanwhile also requiring more independent observations to estimate robustly.

Next, we tested the noise-free scenario for *same*, *diff1* and *diff2* in 3D. Several palpations were applied in spherical coordinates as $u_i = [u_{i,x}, u_{i,y}, u_{i,z}]^T$, with $u_{i,x} = d\sin\theta_i\cos\phi_i$, $u_{i,y} = d\sin\theta_i\sin\phi_i$, and $u_{i,z} = d\cos\theta_i$ for $\theta_i = (\pi i/m)$ and $\phi_i = (\pi i/n)$ with mn being the total number of observations. The average error for m=n=3 are shown in Table I(A) for 3D. As in 2D, *diag* yields minimal error for *same* and *diff1*, but increasing number of linearly-independent observations decreases error for *block* more significantly.

C. Observation Noise

Since displacement observations may be noisy in real applications, we evaluate the effect of noise in our methods. We use uniformly-distributed noise with SNR=20, for which results from an average of 10 different noise experiments are shown in Table I(A) for 2D and 3D numerical phantoms. For increased number of linearly-independent noisy observations, *diag* yields best results. The effect of increased observations M on error in noisy 2D experiments is shown in Fig. 3.

D. Male Pelvic Anatomical Model

For the pelvic model, we used three palpation observations on the skin, and evaluated the accuracy of deformation estimation for displacements applied on the nodes along the needle shaft. We assume that the needle is already inside the model in the stable state, and displacements model the static friction at a "stuck" interaction state [11]. Interactions were simulated by distributing the friction force to the tissue nodes inside a cylindrical region around the shaft with radius R, which was chosen such that there are 8 nodes along the shaft, corresponding to a distribution approximately at the mesh resolution. The external force is distributed to those nodes inversely-proportional to their distance to the needle shaft. Table I(B) shows the average error when 4.5 mm displacement is applied. Since for many applications, such as biopsy and brachytherapy, the location of needle tip is important, we also evaluated errors at the tip. Results show that *diag* yields two times lower error than conventional boundary definition approaches at the needle tip.

TABLE I

AVERAGE ERROR IN 2D AND IN 3D WITH AND WITHOUT NOISE.

(A) Average Error (Phantom)		conventional		CBC			
				noise-free		with noise	
		bottom	*all fix*	*diag*	*block*	*diag*	*block*
2D	*same*	19.5	38.9	**2.0**	2.8	**5.4**	10.5
	diff1			**8.6**	12.3	**11.3**	20.2
	diff2			5.2	**4.6**	**6.5**	12.6
3D	*same*	13.9	29.5	**6.7**	7.2	**7.4**	33.0
	diff1			**7.3**	9.4	23.8	35.1
	diff2			**5.9**	6.5	**6.4**	15.7

(B) Average Error (Male Pelvis)	in %		in mm	
	all nodes	needle tip	all nodes	needle tip
only bone	309.4	349.4	19.2	21.5
all	17.4	31.9	1.1	2.0
diag	**15.8**	**17.8**	**1.0**	**1.1**
block	25.1	19.1	1.5	1.2

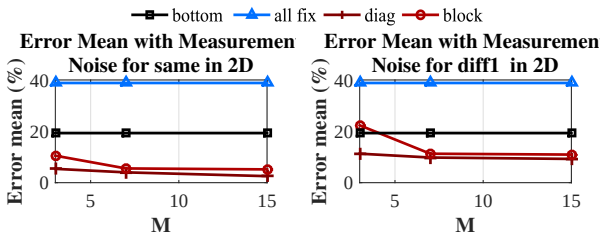

Fig. 3. Using different number of observations in 2D is evaluated. Left plot shows average error for *same* and right plot for *diff1*. For increasing M, average error decreases more significantly for *block*.

IV. CONCLUSIONS AND FUTURE WORK

We presented a novel boundary definition and an observation-based technique to model that. Our proposed method CBC can estimate deformations more accurately than the conventional empirically- or arbitrarily-set boundary conditions. The diagonal approximation of our method is seen to be the effective method. Although CBC requires observations which are not required by conventional approach, it can yield significantly more accurate deformation estimations, essential for clinical settings such as biopsy or brachytherapy simulation. Additionally, in virtual-reality simulations, more accurate boundaries can be incorporated without increasing the computation time, including dynamic or nonlinear models, since the CBC-augmenting a stiffness matrix does not change its size. Next, observations from imaging experiments will be used to study CBC.

REFERENCES

[1] N. Ayache, S. Cotin, H. Delingette, J.-M. Clement, J. Marescaux, and M. Nord. Simulation of endoscopic surgery. *Journal of Minimally Invasive Therapy and Allied Technologies (MITAT)*, 7(2):71–77, 1998.

[2] M. Becker and M. Teschner. Robust and efficient estimation of elasticity parameters using the linear finite element method, 2007.

[3] M. Bro-Nielsen and S. Cotin. Real-time volumetric deformable models for surgery simulation using finite elements and condensation. In *Proceedings of Eurographics*, 1996.

[4] X. Chai et al. Finite element based bladder modeling for image-guided radiotherapy of bladder cancer. *Medical physics*, 38:142–150, 2011.

[5] S. Cotin, H. Delingette, and N. Ayache. Real time volumetric deformable models for surgery simulation. In *Visualization in Biomedical Computing*. Springer Berlin Heidelberg, 1996.

[6] F. Cui, J. Liu, Z. Liu, Y. Chi, J. Liu, J. Wu, T. Qi, and H. S. S. Ho. Predicition of prostate motion and deformation using FE modeling for better biopsy accuracy. In *European Conf. on Comp. Mechanics*, 2014.

[7] E. Dehghan, X. Wen, R. Zahiri-Azar, M. Marchal, and S. Salcudean. Needle-tissue interaction modeling using ultrasound-based motion estimation: Phantom study. *Comp. Aid. Surg.*, 13(5):265–280, 2008.

[8] A.-L. Didier, P.-F. Villard, J. Saade, J.-M. Moreau, M. Beuve, and B. Shariat. A chest wall model based on rib kinematics. In *Proceedings of International Conference on Biomedical Visualization*, 2007.

[9] M. Doyley, P. Meaney, and J. Bamber. Evaluation of an iterative reconstruction method for quantitative elastography. *Physics in Medicine and Biology*, 45(6):1521–1540, 2000.

[10] O. Goksel and S. E. Salcudean. Image-based variational meshing. *IEEE Transactions on Medical Imaging*, 30(1):11–21, 2011.

[11] O. Goksel, K. Sapchuk, and S. E. Salcudean. Haptic simulator for prostate brachytherapy with simulated needle and probe interaction. *IEEE Trans Haptics*, 4:188–198, 2011.

[12] R. M. Koch et al. Simulating facial surgery using finite element models. In *Proceedings of SIGGRAPH*, 1996.

[13] A. Lasso, S. Avni, and G. Fichtinger. Targeting error simulator for image-guided prostate needle placement. In *Procs. of EMBC*, 2010.

[14] S. Misra, K. Macura, K. Ramesh, and A. Okamura. The importance of organ geometry and boundary constraints for planning of medical interventions. *Medical Engineering & Physics*, 31:195–206, 2009.